Implementation of Iwan-Type Nonlinear Rheology in a 3D High-Order Staggered-Grid Finite-Difference Method

Daniel Roten[1] , Te-Yang Yeh[2] , Kim B. Olsen[*2] , Steven M. Day[2] , and Yifeng Cui[1]

─── **ABSTRACT** ───

We have implemented and verified a parallel-series Iwan-type nonlinear model in a 3D fourth-order staggered-grid velocity–stress finite-difference method. The Masing unloading and reloading behavior is simulated by tracking an overlay of concentric von Mises yield surfaces. Lamé parameters and failure stresses pertaining to each surface are calibrated to reproduce the stress–strain backbone curve, which is controlled by the reference strain assigned to a given depth level. The implementation is successfully verified against established codes for 1D and 2D *SH*-wave benchmarks. The capabilities of the method for large-scale nonlinear earthquake modeling are demonstrated for an M_w 7.8 dynamic rupture ShakeOut scenario on the southern San Andreas fault. Although ShakeOut simulations with a single yield surface reduces long-period ground-motion amplitudes by about 25% inside a waveguide in greater Los Angeles, Iwan nonlinearity further reduces the values by a factor of 2. For example, inside the Whittier Narrows corridor spectral accelerations at a period of 3 s are reduced from 1*g* in the linear case to about 0.8 in the bilinear case and to 0.3–0.4*g* in the multisurface Iwan nonlinear case, depending on the choice of reference strain. Normalized shear modulus reductions reach values of up to 50% in the waveguide and up to 75% in the San Bernardino basin at the San Andreas fault. We expect the implementation to be a valuable tool for future nonlinear 3D dynamic rupture and ground-motion simulations in models with coupled source, path, and site effects.

KEY POINTS

- Bilinear yield criteria are inaccurate representations of the stress–strain relationship for most geomaterials.
- Bilinear methods may provide insufficient damping of large-amplitude long-period surface waves.
- Multisurface (compared to bilinear) yield criteria may provide improved nonlinear ground-motion estimates.

Supplemental Material

INTRODUCTION

Strong ground motions during earthquakes are the result of wave propagation phenomena that occur over a wide range of scale lengths, from hundreds of kilometers (e.g., due to source directivity effects) to a few tens of meters for local site effects. These phenomena can be modeled using simulations of dynamic rupture and wave propagation via various sophisticated and scalable 3D numerical methods, aided by the availability of computational resources (e.g., Tu *et al.*, 2006; de la Puenta *et al.*, 2008; Cui *et al.*, 2010, 2013). An example of important results obtained from such large-scale simulations of wave phenomena is the potential waveguide from interconnected sedimentary basins in the Los Angeles area (Olsen *et al.*, 2006, 2008, 2009; Graves *et al.*, 2008; Roten *et al.*, 2011).

Although these large-scale 3D simulations assumed linear rheology, it is well known that waves with sufficiently large amplitudes propagating into soft, usually near-surface earth material are affected by nonlinear behavior. The effects of nonlinear behavior on the seismic ground motion include damping of amplitudes and shift of resonance peaks toward lower frequencies (e.g., Rajaure *et al.*, 2017; Castro-Cruz *et al.*, 2020). Conventionally, nonlinear analysis of ground motions have been conducted based on shear modulus reduction curves following the Masing criterion (Masing, 1926) to describe

---

Cite this article as Roten, D., T.-Y. Yeh, K. B. Olsen, S. M. Day, and Y. Cui (2023). Implementation of Iwan-Type Nonlinear Rheology in a 3D High-Order Staggered-Grid Finite-Difference Method, *Bull. Seismol. Soc. Am.* **XX**, 1–17, doi: 10.1785/0120230011.

unloading and reloading, often for 1D near-surface, vertical wave propagation models (e.g., Regnier et al., 2016, 2018). However, due to significant computational requirements for these methods, other approximate nonlinear schemes have been developed, including the equivalent-linear method (Seed and Idriss, 1969), nonlinear viscoelastic schemes (e.g., Delépine et al., 2009), elasto-plastic schemes (e.g., Amorosi et al., 2016), and poroelastoplastic schemes (e.g., Blanc et al., 2013). Fully hysteretic nonlinear simulations of soft soils have usually been limited to the earth structure underlying a site of interest, or depended on simplifying assumptions, such as a laterally homogeneous structure and a vertically incident wavefield (e.g., Griffith and Prevost, 1988). The decoupled analysis of source, path, and site effects generally employed in these studies, also known as site response formalism (Sleep and Erickson, 2014), neglects the important interplay between multidimensional and potentially nonlinear effects caused by phenomena such as long-period surface waves, finite-fault effects, and fault damage zones. The traditional treatment of source, path, and site effects as decoupled processes is becoming increasingly untenable for large events as model complexity and frequency range increase. Instead, a paradigm shift from using empirical ground motions to physics-based time histories for which the response of the entire shallow crust is treated as a coupled, dynamical system (Bradley, 2018) is now feasible.

The implementation of Mohr–Coulomb and Drucker–Prager (DP) rheology in dynamic rupture and wave propagation codes has enabled studies of nonlinearity in fault damages zones (Andrews et al., 2007; Ma, 2008; Gabriel et al., 2013; Roten, Olsen, et al., 2017), in path effects (Roten et al., 2014; Roten, Cui, et al., 2016; Roten, Olsen, et al., 2016; Wollherr et al., 2018, 2019), and in 3D sedimentary basins (Xu et al., 2003; Taborda et al., 2012). Such simple bilinear yield criteria have tremendously improved our understanding of the 3D nature of nonlinear wave propagation in heterogeneous media and offered insights into the strong coupling between structural complexity, rupture dynamics, propagation path, and local site response. For example, it has been shown that plastic deformation of rocks in the damage zone can mitigate effects of forward directivity (Roten et al., 2014; Wollherr et al., 2019) and modify ground motions at much longer periods than previously supposed. Moreover, dynamic rupture simulations with bilinear (e.g., elastic–plastic or viscoelastic–plastic) rheology have demonstrated that fault-zone plasticity contributes to shallow slip deficit and off-fault deformation (Kaneko and Fialko, 2011; Roten, Olsen, and Day, 2017; Wollherr et al., 2019) observed during the past earthquakes.

On the other hand, bilinear rheology is not an accurate representation of the stress–strain relationship of most geomaterials. This is illustrated schematically in Figure S1, available in the supplemental material to this article, which compares the stress–strain path in simple shear for the uniaxial case. In the Mohr–Coulomb yield condition, the stress–strain relationship remains linear until the yield stress is reached (see Fig. S1a for

further details). Laboratory experiments, however, indicate a gradual reduction of the shear modulus (e.g., Hardin and Drnevich, 1972) and a reduction in the slope of the stress–strain curve with increasing strain. The bilinear stress–strain approximation leads to inflated hysteresis loops, which may bias damping of the ground motion in the course of many stress–strain cycles (Kramer, 1996).

To more realistically represent the cyclic response of geomaterials in 3D wave propagation, we describe the implementation and verification of a multisurface, nonlinear model in a fourth-order staggered-grid finite-difference code. We verify the code in 1D and 2D media against well-established nonlinear, hysteretic codes. Important applications of such method include the simulation of large scenario earthquakes, for which an important part of the seismic hazard is controlled by nonlinear attenuation in soft, near-surface sediments. An example of such large-scale application is the ShakeOut scenario (Jones et al., 2008), which assumes a northwestward rupturing M 7.8 earthquake on the southern San Andreas fault (SSAF). Ground motions obtained from simulations of the ShakeOut scenario have shown that a string of contiguous sedimentary basins between the SSAF and the Los Angeles basin (LAB) would act as a waveguide and channel amplified long-period surface waves into densely populated urban areas (e.g., Olsen et al., 2006, 2009; Graves et al., 2008; Bielak et al., 2010). Furthermore, amplification effects that have been linked to this waveguide effect have also been confirmed from independent observations in the form of virtual earthquakes (Denolle et al., 2013), which were constructed using Green's functions derived from the ambient seismic field.

However, subsequent simulations of the M 7.8 ShakeOut scenario for a nonlinear medium with a DP (viscoelastic–plastic) yield condition predicted long-period (>1 s) shaking levels that were significantly lower in the LAB than the corresponding linear solutions (Roten et al., 2014). These reductions were caused by both nonlinear attenuation of long-period surface waves (e.g., Joyner, 2000; Sleep, 2010, 2014; Sleep and Erickson, 2014) and near-fault plasticity effects (e.g., Andrews, 2005; Ma, 2008; Duan and Day, 2010; Harris et al., 2011). The recent high-resolution simulations of an M 7.7 earthquake on the SSAF found even stronger nonlinear effects (Roten, Cui, et al., 2016; Roten, Olsen, et al., 2016) at higher frequencies (2 Hz) and concluded that nonlinearity must be included to bring simulated near-fault accelerations in line with ground-motion prediction equations, even at frequencies less than 1 Hz.

To demonstrate the large-scale capabilities of our multisurface nonlinear implementation, and to compare the strength of nonlinear damping obtained using a single (e.g., Roten et al., 2014) and multiple yield surfaces, we simulate a variation of the M 7.8 ShakeOut scenario with a dynamic rupture source. Furthermore, we quantify the variation in the resulting ground-motion amplification, including in the inferred waveguide, due to uncertainty in the nonlinear parameters.

IWAN NONLINEAR MODEL

The idea behind the Iwan nonlinear model is that a material governed by hysteretic behavior can be thought of as a large number of elastic, perfectly plastic components having different yield levels. In the 1D (uniaxial) case, this can be illustrated using an assembly of elastic springs and plastic sliders, which can either be arranged in a series-parallel or parallel-series configuration. Each single spring–slider combination obeys an ideal elastoplastic stress–strain relationship (see Fig. S2).

Kaklamanos et al. (2015) described the implementation of a parallel-series model based on the overlay concept (Nelson and Dorfmann, 1995) in a 1D finite-element code (see Fig. S3 for illustration of the approach for three parallel elements), and Santisi d'Avila et al. (2019, 2012), Santisi d'Avila and Semblat (2014), and Santisi d'Avila et al. (2013) presented nonlinear modeling results for one-directional, three-component Iwan-type models. The stresses associated with the individual parallel elements, all subject to the same deformation, add up to the total stress–strain curve of the material. The stress–strain variation of each element (i) is elastic with shear modulus G_i for strains less than γ_i and behaves perfectly plastically with yield stress τ_{γ_i} when strains exceed γ_i. The total stress–strain variation is given by a number of yield points occurring at increasingly higher strain values—a behavior that approaches the backbone curve $\tau = f(\gamma)$. In this way, the total shear stress τ at a given shear strain γ is given by the sum of elastic and plastic terms:

$$\tau(\gamma) = \sum_{i=1}^{n} G_i \gamma + \sum_{i=n+1}^{N} \tau_{\gamma i}, \tag{1}$$

in which the number of elements n will stay elastic up to strain γ, with N denoting the total number of elements. In this way, τ is the sum of the shear moduli of the individual elements. Thus, as strain increases, more elements are forced to yield, causing the load to be supported by a smaller number of elastic elements, while G decreases. When the last element turns nonlinear, the load cannot increase any further. We will refer to this as an overlay model, which corresponds to the multiyield-surface J2 (or von Mises) plasticity described by Iwan (1967) and Mroz (1967).

The strength of the earth material is controlled by the reference strain γ_r, which is defined as the strain for which the shear modulus reduction curve reaches half of the low-strain value. Iwan (1967) and Mroz (1967) showed that the combined system of spring–slider elements follows a hyperbolic path, in agreement with the Masing (1926) criteria, which are frequently used to describe the behavior of soils under cyclic loading (e.g., Kramer, 1996; see Fig. S4 for a comparison of a reference backbone and shear modulus reduction curve, computed for a reference strain of $\gamma_r = 10^{-3}$, with the values approximated by seven yield surfaces).

Although Iwan (1967) focused on the series-parallel model to extend this approach to 3D, later studies on multiaxial cyclic plasticity (Chiang, 1992; Chiang and Beck, 1994; Einav, 2005;

Einav and Collins, 2008) demonstrated that a much simpler 3D model can be developed based on the parallel-series model. In this approach, the yield surfaces of individual components remain fixed, eliminating the need for moving the nested yield surfaces and preventing them from overlapping. The parallel-series model has successfully been used for continuum modeling (Dawson et al., 2013) and seismic-wave propagation (Kaklamanos et al., 2015). Here, we also use a parallel-series model to simulate soil nonlinearity, to be referred to as the Iwan model in the following.

IMPLEMENTATION DETAILS

We implement the Iwan nonlinear rheology in the explicit, fourth-order velocity–stress staggered-grid finite-difference code Anelastic Wave Propagation–ODC, with suffix derived from the authors Olsen, Day, and Cui. AWP-ODC solves the 3D elastodynamic equations, including frequency-dependent anelasticity (Withers et al., 2015), using memory variables. The code has near-perfect scaling on both central processing unit (CPU) computers (Cui et al., 2010) and graphic processing unit (GPU) computers (Cui et al., 2013), and the code is a widely used community modeling tool used for research into the dynamics and hazards of earthquakes, as well as for engineering research (Graves et al., 2010; Crouse et al., 2018). AWP-ODC was used to demonstrate, among other applications, nonlinear damping in fault zones (Roten, Olsen, et al., 2017), and off-fault deformation and shallow-slip deficit (Roten, Olsen, and Day, 2017) using a bilinear (DP) yield condition. In the following, we describe the implementation of Iwan nonlinearity in AWP-ODC, referred to in the following as AWP-ODC-Iwan.

Tracking stresses pertaining to multiple yield surfaces

AWP-ODC-Iwan tracks a series of von Mises yield surfaces (elements) arranged in a parallel-series configuration. Each element n is characterized by its Lamé parameters (μ_n and λ_n) and its yield stress τ_n. At each timestep in the simulation, the current stress σ_n associated with element n must be known. This requires a separate copy of the array storing the stress tensor for each element, which increases memory requirements. Because all elements share the same strain in the parallel-series configuration, the three-component velocity field and densities are also shared by all elements.

During each iteration, a separate stress update is performed for each element based on the element's Lamé parameters and the particle velocity $\mathbf{v}$:

$$\sigma^{(n)}(t + \Delta t) = \sigma^{(n)}(t) + \Delta t (\lambda_n (\nabla \cdot \mathbf{v}) I + \mu_n (\nabla \mathbf{v} + \nabla \mathbf{v}^T)), \tag{2}$$

in which $\sigma^{(n)}(t + \Delta t)$ is the updated stress tensor for element n, and $\sigma^{(n)}(t)$ is the element's stress tensor from the previous timestep, and '·' depicts dot product. A plasticity update is

carried out independently for each element n using the return map algorithm (Wilkins, 1964; Simo and Taylor, 1986):

$$F(\sigma^{(n)}) = \sqrt{J_2(\sigma^{(n)})} - \tau_n \leq 0, \tag{3}$$

in which $J_2 = \frac{1}{2}\sum_{i,j}s_{ij}^{(n)}s_{ji}^{(n)}$ is the second invariant of the stress deviator $s_{ij}^{(n)} = \sigma_{ij}^{(n)} - \sigma_m^{(n)}\delta_{ij}$ for element n, with mean stress $\sigma_m^{(n)} = \frac{1}{3}(\sigma_{xx}^{(n)} + \sigma_{yy}^{(n)} + \sigma_{zz}^{(n)})$ and Kronecker delta δ_{ij}. If the yield condition is exceeded ($F(\sigma^{(n)}) > 0$), the element yields in shear, and the stress is reduced to:

$$\sigma_{ij}^{(n)'} = \sigma_m^{(n)} + \delta_{ij}r^{(n)}s_{ij}^{(n)}. \tag{4}$$

The variable $r^{(n)}$ is the yield factor for element n, and defined as the ratio between the yield stress and the square root of J_2 before the plasticity update:

$$r^{(n)} = \frac{\tau_n}{\sqrt{J_2(\sigma^{(n)})}}. \tag{5}$$

The earlier value for r is used in a pure elastoplastic simulation. In a viscoplastic simulation, a viscoplastic relaxation term is added:

$$r_{vp} = r^{(n)} + (1 - r^{(n)})e^{\frac{-\Delta t}{t_v}}. \tag{6}$$

The viscoplastic relaxation time t_v is set to the time it takes for an S wave to travel through one element $t_v = \Delta h/v_s$ and is needed to stabilize the solution (Andrews, 2005). After the stress and plasticity updates have been performed for each element, the overlay stress tensor is computed (Fig. S5) by summation of the stress tensors associated with each element:

$$\sigma_{ij}^{(O)} = \sum_{n=1}^{N}\sigma_{ij}^{(n)}. \tag{7}$$

The velocity field for the next timestep is then computed from the overlay stress field, just as in a regular elastic or single-surface elastoplastic simulation. See Figure S5 for a flow chart describing the implementation of the Iwan model in AWP.

AWP-ODC-Iwan uses 4D arrays to store the six independent components of the stress tensor, with three dimensions reflecting the 3D geometry of the medium and the fourth dimension representing the number of the element associated with the stress tensor. The 4D arrays are also required for the two Lamé parameters λ and μ and the yield stress $\tau_{\max}$, which are computed for each yield surface following Kaklamanos *et al.* (2015). Velocity vectors and densities are stored in 3D arrays, and velocity updates are computed from the compound (overlay) stress tensor, which is obtained by summation over the individual stress tensors.

The version of AWP-ODC-Iwan adapted to CPU platforms uses message passing interface (MPI) and geological domain decomposition to distribute the computational cost over computing nodes (Cui *et al.*, 2010), and both stresses and velocities within two-layer ghost cell regions are exchanged with adjacent subdomains after each stress and velocity update. Similarly, the GPU-powered version of AWP-ODC uses MPI and domain decomposition to distribute the computational load over multiple GPUs. Velocity, stress, and plasticity updates are carried out in parallel using several streaming multiprocessors on each GPU. The GPU version of AWP-ODC uses four ghost cell layers and no stresses are swapped (Cui *et al.*, 2013); therefore, the additional stress tensors used for multisurface plasticity do not result in additional MPI communication in the GPU version of AWP-ODC-Iwan. To conserve often limited memory space on GPU platforms, multiple parameters (such as each spring's Lamé parameters and yield stress) are recomputed on the fly during each iteration and are not stored. Because stencil codes such as AWP are memory bound, the additional computational cost of this memory optimization strategy is minimal (Roten, Cui, *et al.*, 2016). However, in the CPU version of AWP-ODC, the additional stress tensors required to track different yield surfaces result in additional communication, which reduces the parallel efficiency of the code during very large simulations. For example, we recorded a parallel efficiency of 77% using 430,080 MPI processes on the system Frontera at Texas Advanced Computing Center.

The accuracy of the nonlinear response calculation from the Iwan method increases with the number of yield surfaces included. In the Discussion and Conclusions section, we present a convergence test as a function of the number of yield surfaces involved. The test shows that the accuracy increases up to about 10 yield surfaces, with little accuracy gained by adding additional surfaces. Based on this result, we carry out our verification tests and large-scale SSAF simulations in the following using at least 10 yield surfaces.

Boundary conditions

In addition to calculation of the stresses in the internal part of the computational volume, stress updates for each element are required inside the absorbing boundary regions, at the free surface and for source insertion. AWP-ODC-Iwan supports both perfectly matched layers (PMLs; Marcinkovich and Olsen, 2003) using wavefield splitting and sponge zones (Cerjan *et al.*, 1985). Because of the added numerical complexity related to the wavefield splitting procedure, Iwan plasticity is not implemented inside the PMLs. On the other hand, Iwan plasticity is implemented inside the Cerjan absorbing boundaries, for which the attenuation term is applied individually to the stress field for each element as well as to the overlay stress field.

The free surface is defined at the same staggered-grid depth level as the shear stresses σ_{xz} and σ_{yz}, corresponding to free-surface boundary condition "FS2" described by Gottschämmer

and Olsen (2001). In this method, the stress tensor components defined exactly at the free surface are set to zero, and calculating those located above the free surface using antisymmetry. In AWP-ODC-Iwan, we enforce these conditions individually for each element n:

$$\tau_{xz}^{(n)}(k = 0) = 0,$$
$$\tau_{zz}^{(n)}(k = -1/2) = -\tau_{zz}^{(n)}(k = 1/2),$$
$$\tau_{xz}^{(n)}(k = -1) = -\tau_{xz}^{(n)}(k = 1),$$
$$\tau_{yz}^{(n)}(k = -1) = -\tau_{yz}^{(n)}(k = 1).$$

Here, k denotes the position of the free surface in a coordinate system with positive down.

Seismic source definition

Kinematic sources are implemented in AWP-ODC by adding the time-dependent moment rate at predefined source locations (subfaults) to the stress tensor (Olsen and Archuleta, 1996). For AWP-ODC-Iwan, this is done individually for each stress element n. Moment rates M_{ij} are distributed over the respective elements proportionally to their Lamé parameters:

$$\sigma_{ij}^{(n)}(t^+) = \sigma_{ij}^{(n)}(t^-) - \frac{\Delta t}{\Delta h^3} M_{ij}(t) \frac{\mu_n}{\mu_O}, \qquad (8)$$

in which t^- denotes the time before the source insertion, and t^+ denotes the time after the source insertion. The overlay shear modulus is the physical shear modulus and is the sum of each element's shear modulus. Normalizing the source functions by μ_O is required, as the moment rates M_{ij} provided as input already reflects the shear modulus at the subfault location,

$$\mu_O = \sum_{n=1}^{N} \mu_n. \qquad (9)$$

Note that $\mu_n/\mu_O = \lambda_n/\lambda_O$, because each element has the same Poisson ratio.

AWP-ODC also supports dynamic rupture propagation on planar fault surfaces using the staggered-grid split-node (SGSN) method (Dalguer and Day, 2007; Roten, Cui, et al., 2016), which has been verified against other dynamic rupture propagation methods within the Southern California Earthquake Center dynamic rupture code verification exercise (Harris et al., 2009, 2011, 2018) for the linear and nonlinear (DP) case. The code supports a vertical, planar fault parallel to the X-axis, intersecting the positions where the normal stresses and the shear stress σ_{xz} are defined. The implementation defines split nodes for the normal stresses σ_{zz}, σ_{xx}, the shear stress τ_{xz}, and the velocities v_x and v_z on adjacent sides of the fault. A second-order accurate finite-difference update is used to approximate gradients at grid points less than two grid spacings from the fault. Within this zone

surrounding the fault plane, the yield condition is evaluated individually at every location where a shear or normal stress component is defined on the staggered grid (Roten, Cui, et al., 2016). With Iwan rheology, the yield condition is evaluated for the stress tensor associated with each yield surface, and the overlay stress is computed before the second-order updates of the velocity. Shear tractions arising from spontaneous rupture are distributed over the individual elements proportionally to the element's Lamé parameters in the same way as moment rates are distributed over the individual elements for kinematic sources (equation 8). In dynamic rupture mode, the code allocates additional stress arrays for the zone surrounding the fault, expanding the arrays to 4D. Because the ghost cell regions of these fault zone stress arrays are swapped with adjacent subdomains during each iteration, stress exchange subroutines pertaining to dynamic rupture were also adjusted to accommodate these expanded stress arrays.
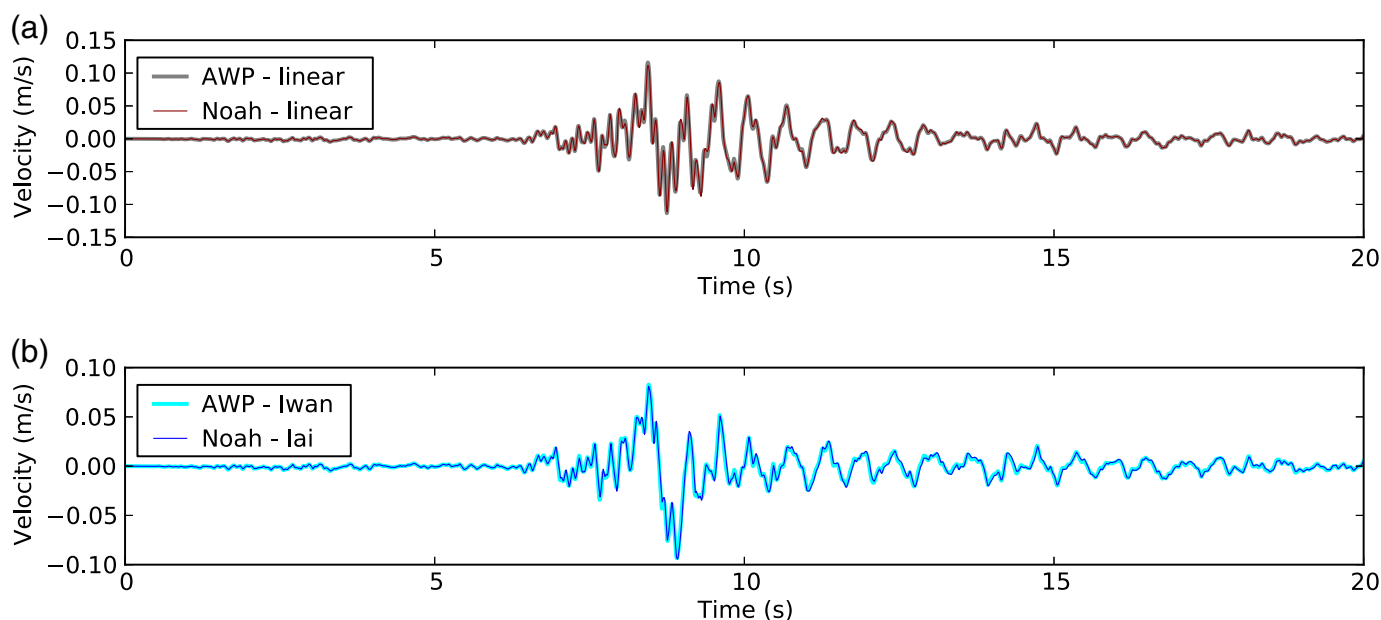
VERIFICATION OF AWP-ODC-IWAN

To verify that AWP-ODC-Iwan produces accurate results, we compared synthetics against reference solutions from 1D and 2D benchmarks. The Noah and Noah2D programs (Bonilla et al., 2005, 2006) are well suited to compute reference solutions, because they have been verified against many other nonlinear codes and validated against observations within the PRENOLIN project (Régnier et al., 2018).

Periodic boundary conditions and plane-wave sources

To efficiently simulate nonlinear response in a small-size 1D medium due to an impinging plane-wave source, we added the option to use periodic boundary conditions at the lateral edges of the domain in AWP-ODC-Iwan. We also enabled an option for defining a vertically incident plane-wave seismic source (plane-strain) in AWP-ODC-Iwan, imposed at the bottom of the computational domain. In addition to verification and validation applications, this feature is useful for site response calculations.

Verification for 1D case

We performed a 1D simulation of vertical wave propagation using the velocity structure at the KiK-net site KSRH10, which was used as one of the two test sites in the PRENOLIN project (Régnier et al., 2018). The downhole east–west seismogram of an M 6 earthquake recorded on 29 November 2004 was used as the (plane wave) input signal. The simulation was carried out for a viscoelastic linear medium and a nonlinear medium represented by 20 yield surfaces (Fig. 1), which is sufficient for an accurate solution (see the Discussion and Conclusions section). We computed reference solutions using the Noah (Bonilla et al., 2005) code for linear and nonlinear cases using the strain-space multi-shear plasticity model (Iai et al., 1992). We used a grid spacing of $\Delta h = 1$ m for both AWP-ODC-Iwan and Noah. The reference

Figure 1. Comparison of simulated surface velocity time series at KiK-net site KSRH10 obtained with AWP-ODC-Iwan and Noah in (a) linear (viscoelastic) and (b) nonlinear cases. The color version of this figure is available only in the electronic edition.

strain γ_r was used to control the strength of the soils in both AWP-ODC-Iwan and Noah simulations. We derived the reference strain from the shear strength τ_{max}, which was computed from friction angles and cohesion provided for the site KSRH10 in Régnier *et al.* (2015). *S*-wave velocities, densities, and quality factors were also adopted from Régnier *et al.* (2015; see Fig. S6). As expected, solutions are virtually identical in the linear case (Fig. 1a). In addition, time series obtained with AWP-ODC-Iwan closely follow the reference solution obtained with Noah using the generalized Masing rules (Fig. 1b). Surface-to-borehole transfer functions (Fig. 2) obtained with AWP-ODC-Iwan are also consistent with the reference solutions, predicting a similar reduction in amplitude and shift of resonance frequencies (small differences likely caused by different implementations of anelastic attenuation). Table 1 lists the modeling parameters for the 1D benchmark. The model parameters provide a resolution of at least 14 points per wavelength at the maximum frequency of 10 Hz to accommodate reduction of the shear modulus in the nonlinear case. Finally, Figure S7 shows good agreement between transfer functions, Fourier amplitude spectra (FAS), and resulting time series for AWP and theoretical solutions for the linear case.

Verification for 2D case

To analyze the performance of AWP-ODC-Iwan in the presence of lateral heterogeneities, we carried out a 2D simulation of *SH* wave propagation for a generic sediment-filled valley and compared the results to those from the code Noah2D (Bonilla *et al.,* 2006). We specified the sediment–bedrock interface with a constant slope on the left side and sine-shaped on the right side (Fig. 3b), with a shear-wave velocity of 3200 m/s in bedrock and 200 m/s at the surface of the basin, resulting in a relatively high-velocity contrast. The sediments within the basin are layered horizontally, and velocities and densities are constant inside each

layer. The shear-wave velocity reaches 750 m/s in the lowermost layer. We specified a reference strain of $\gamma_r = 10^{-3}$ in the uppermost layer, $\gamma_r = 5 \times 10^{-3}$ in the second layer (50–100 m depth), and $\gamma_r = 10^{-2}$ in the third layer (100–200 m depth). The basin was excited using a vertically propagating, planar shear-wave source with transverse particle motion (horizontal direction in Fig. 3b, perpendicular to the basin axis), and a Ricker wavelet with a center frequency of 3 Hz was used as source time function. Unfortunately, the implementation of viscoelastic attenuation in
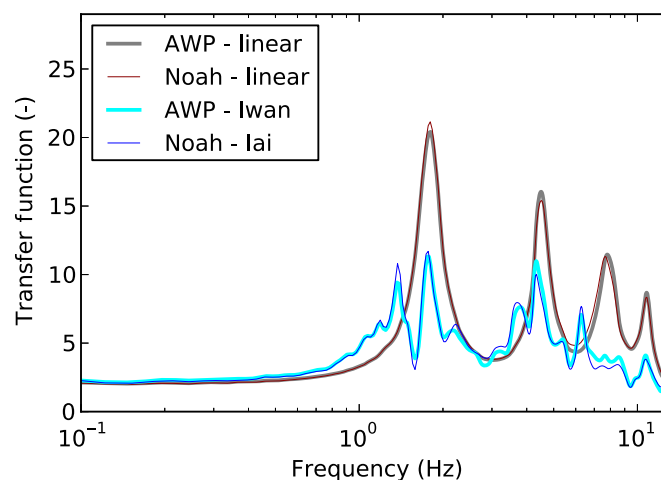

Figure 2. Surface-to-borehole Fourier transfer functions at KSRH10 obtained using AWP-ODC-Iwan and Noah. The color version of this figure is available only in the electronic edition.
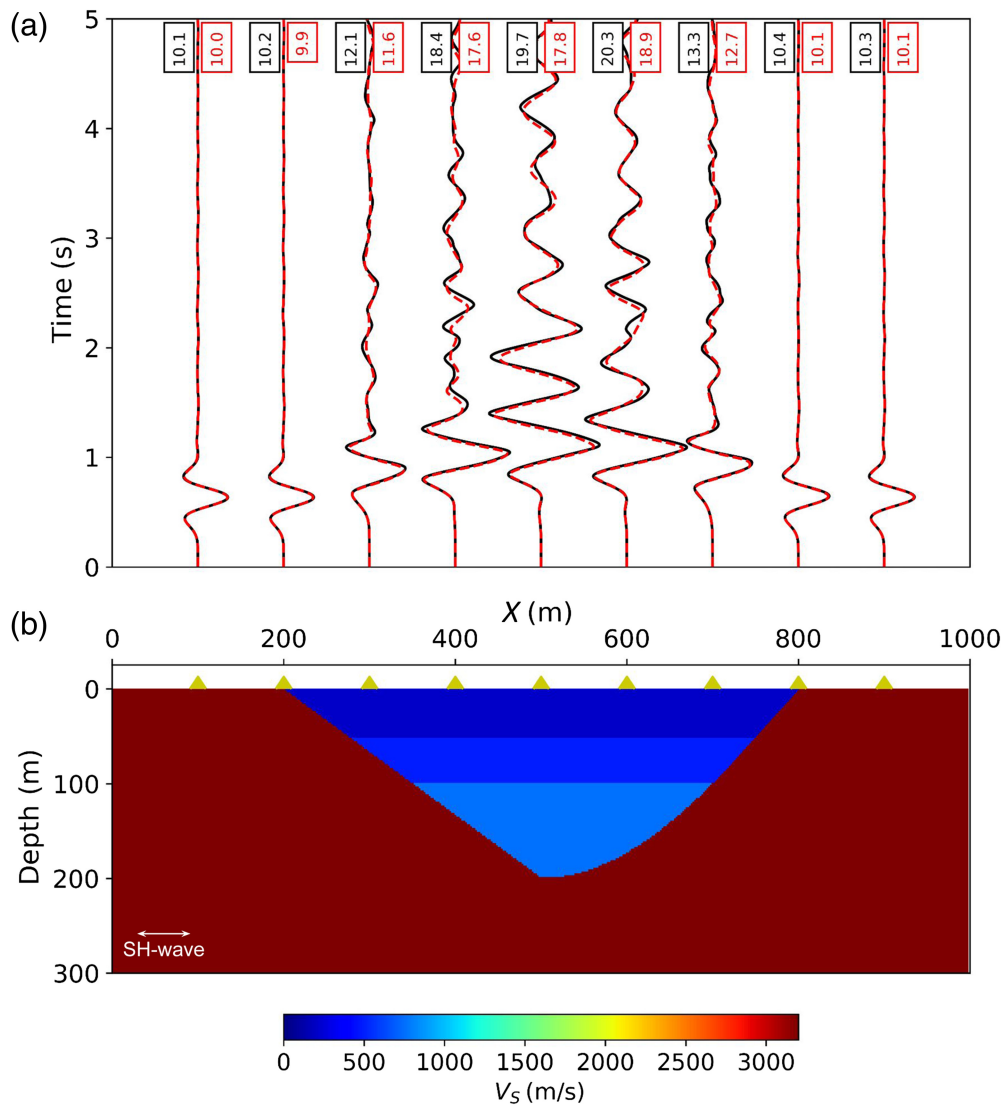
Figure 3. (a) Comparison of transverse velocity time series obtained from 2D nonlinear *SH*-wave propagation inside a sediment-filled valley. Dashed and solid wiggles show the solutions obtained with AWP-ODC-Iwan and Noah2D, respectively. (b) Shear-velocity and location of plotted stations (triangles). The arrow indicates the polarization of the *SH*-wave source. The color version of this figure is available only in the electronic edition.

instabilities with the Q implementation were recorded in AWP-ODC-Iwan for linear or nonlinear computations. Table 2 lists the modeling parameters for the 2D benchmark.

Figure 3a compares the ground motions obtained with AWP-ODC-Iwan and Noah2D in the nonlinear case, revealing time series very similar in shape and amplitude. In both codes, peak velocities in the center of the basin are reduced from 38 cm/s in the linear case (not shown) to about 20 cm/s in the nonlinear case. In addition, the nonlinearity greatly reduces the duration of the shaking, and this feature is also reproduced well by AWP-ODC-Iwan. The small misfit is likely caused by differences in the implementation of boundary conditions, media parameter averaging, as well as the nonlinear rheology in the two codes.

The 2D verification confirms that the Iwan multisurface method works as expected in AWP-ODC. Because of the lack of available 3D nonlinear wave propagation codes and benchmarks, no verification of AWP-ODC-Iwan in the 3D case has been performed so far. For additional insight into the 2D verification case (accumulated strain, minimum G/G_{max}, and hysteretic depth-dependent stress–strain variation), see Figure S8.

Noah2D based on a generalized Maxwell body (e.g., Nowick and Berry, 1972) results in numerical instabilities near the strong lateral velocity contrasts at the basin edges (Fabian Bonilla, written comm., 2023). Therefore, the verification for the 2D case was performed without including anelastic losses in the computation. No

SHAKEOUT SCENARIO WITH IWAN NONLINEAR RHEOLOGY

To demonstrate the capabilities of AWP-ODC-Iwan for large-scale ground-motion modeling, we simulate a *M* 7.8 ShakeOut scenario event on the SSAF with 10 yield surfaces. Rupture propagation is simulated from southeast to northwest to obtain the maximum excitation of the waveguide due interconnected basins in the northern Los Angeles area (Olsen *et al.*, 2006; Graves *et al.*, 2008; Olsen *et al.*, 2008, 2009). We use a scenario simulated dynamically with the SGSN technique (Dalguer and Day, 2007) on a 250 km long stretch of the SSAF using a vertical,
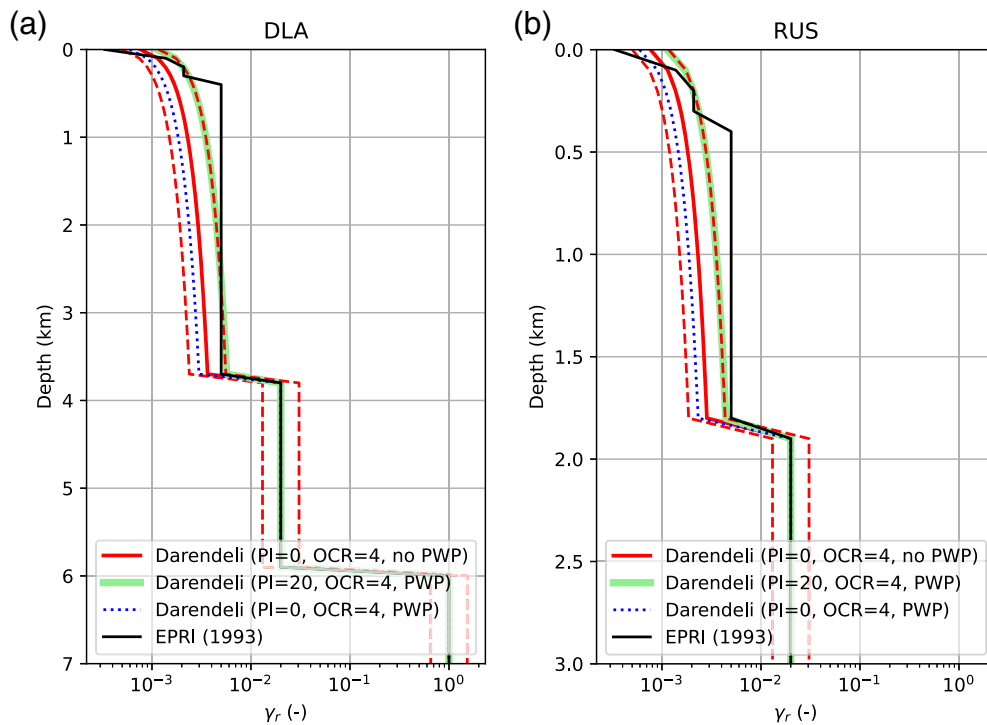
TABLE 1	
Simulation Parameters for 1D Verification Case	
Grid spacing	1 m
Maximum frequency	10 Hz
Minimum V_S	140 m/s
Timestep	0.000125 s
Simulation time	20 s

Figure 4. Reference strain γ_r as a function of depth at strong-motion sites (a) downtown Los Angeles (DLA) and (b) RUS. The solutions are obtained with the Darendeli (2001) relationship using different assumptions for the plasticity index (PI), with or without pore water pressure (PWP) effects, and using the Electric Power Research Institute (EPRI; Electric Power Research Institute, 1993) shear modulus reduction curves. Dashed blue lines show the reference strain obtained by adding or subtracting one standard deviation from the reference strain shown in the solid blue line. OCR, overconsolidation ratio. The color version of this figure is available only in the electronic edition.

planar fault approximation, with a random stress field to mimic fault roughness. The scenario has a stress drop of 7.1 MPa and maximum slip of 6 m (see Roten, Cui, et al., 2016 for additional details of the source parameters. In addition, we explore the sensitivity of ground motions in the LAB to the strength (in terms of the reference strain) of the sedimentary deposits.

Definition of reference strain

For the ShakeOut scenario, we use an empirical relationship (Darendeli, 2001) to assign the reference strain as a function of depth, for which the reference strain is assigned as a function of plasticity index (PI), over-consolidation ratio (OCR), and mean effective confining pressure σ_0':

$$\gamma_r = (\phi_1 + \phi_2 \times \mathrm{PI} \\ \times \mathrm{OCR}^{\phi_3})\sigma_0'^{\phi_4}. \quad (10)$$

We used the tabulated mean values for the four soil groups analyzed by Darendeli (2001) to define the parameters $\phi_1 - \phi_4$. We assumed a value of 0 for the PI (i.e., no clay content) and a value of 4 for the OCR, which corresponds to isotropic consolidation (i.e., coefficient of earth at rest $K_0 = 1$). It is noted that the OCR in the Darendeli relationship has no effect on γ_r if PI = 0. If we neglect pore water pressure (PWP) effects for the computation of the effective vertical stress, the reference strain ranges from $\gamma_r = 0.8 \times 10^{-4}$ at the surface to $\gamma_r \approx 2 \times 10^{-2}$ at 4 km depth (Fig. 4). Outside the basins, we assigned a value of $\gamma_r = 2\%$ for rock (Schnabel et al., 1972). At depths larger than 6 km, we set a reference strain of 100%, effectively prohibiting nonlinearity (Fig. 4a).

Definition of initial stress

In nonlinear wave propagation simulations, the absolute value of the initial stress needs to be defined. We distinguish between hard-rock sites with surface $V_S > 1950$ m/s and sediment sites with surface $V_S \leq 1950$ m/s. For regions inside rock, we follow the initial stress definition used by Ma (2008), Roten, Olsen, et al. (2017) and Roten, Olsen, and Day (2017), and assume that the major principal stress σ_1 is rotated by 45° with respect to the fault, with relations between principal stresses of $\sigma_1 = 1.4 \, \sigma_2$ and $\sigma_2 = 0.6 \, \sigma_3$. The intermediate principal stress σ_2 is taken as vertical and computed from the lithostatic load. Inside the sedimentary basins, we assume hydrostatic stress conditions (Bethke, 1986), with $\sigma_1 = \sigma_2 = \sigma_3$.

A complication arises from the hysteretic stress–strain relationship in the Iwan model, because the position in stress–strain space is not uniquely defined by the initial stress (i.e., the strain can not be inferred from the stress). A few of the weaker sliders in the spring–slider assembly typically reach their yield value if the configuration is loaded to realistic initial stress. Here, we define the initial state of the individual stress tensors using

TABLE 2	
Simulation Parameters for 2D Verification Case	
Grid spacing	1 m
Maximum frequency	10 Hz
Minimum V_S	200 m/s
V_S, ρ, thickness, γ_r (layer 1)	200 m/s, 1800 kg/m³, 50 m, 0.001
V_S, ρ, thickness, γ_r (layer 2)	500 m/s, 2000 kg/m³, 50 m, 0.005
V_S, ρ, thickness, γ_r (layer 3)	750 m/s, 2200 kg/m³, 100 m, 0.01
V_S, ρ, γ_r (rock)	3200 m/s, 2500 kg/m³, 100 (linear)
Points per minimum wavelength	10
Timestep	0.000125 s
Simulation time	5 s

Grid spacing	100 m
Maximum frequency	1 Hz
Minimum V_S	500 m/s
Rock intermediate principal stress σ_2*	Vertical, calculated from lithostatic load
Rock maximum principal stress σ_1*	1.4 σ_2, rotated 45° with respect to SAF
Rock minimum principal stress σ_3*	1.4 σ_2
Sediments $\sigma_1, \sigma_2, \sigma_3$	$\sigma_1 = \sigma_2 = \sigma_3$, hydrostatic conditions
Simulation time	100 s

*Rock and sediments are defined as material with $V_s > 1950$ and $V_s < 1959$, respectively.

an iterative procedure, for which the initial stress is first distributed over the different spring–slider elements proportionally to their shear moduli (spring constant). If the resulting stress is below the target value due to yielding of one or more elements, the residual stress is distributed over the remaining (nonyielding) spring–slider elements, and the procedure is repeated until the target stress is reached. For the ShakeOut simulations, initial loading was performed to 1.5 times the target stress (50% overshoot), and each spring was subsequently relaxed proportionally to its strength at the target stress. This approach avoids initial stress tensors touching their yield surface at the beginning of the simulation, and reflects loading and subsequent unloading of the medium during previous events. Table 3 lists the modeling parameters for the ShakeOut scenario.

Ground-motion predictions

As shown in many previous studies (Graves *et al.*, 2008; Olsen *et al.*, 2008, 2009; Roten, Olsen, *et al.*, 2016), simulations of the ShakeOut scenario predict large long-period ground motions inside the waveguide connecting the SSAF to the LAB. For example, spectral accelerations at a period of 3 s (SA-3s) reach values of more than 1g in the linear case (Fig. 5a) for our ShakeOut scenario. However, if nonlinearity based on the Iwan model is taken into account, using the reference strain predicted by the Darendeli relationship (PI = 0, no PWP effects), SA-3s values are reduced by about a factor of 2–3 inside the waveguide (see Fig. 5b).

Variation of ground motions due to uncertainty in nonlinear parameters

In this section, we investigate the sensitivity of the simulated ground motions to the choice of nonlinear parameters in the Iwan rheology for the ShakeOut scenario. In addition, we compare the ground motions obtained from a simulation with AWP-ODC-Iwan using 10 yield surfaces to those from a single yield surface. Finally, we test another procedure for defining depth-dependent reference strains, following the Electric

Power Research Institute (EPRI93) shear modulus reduction curves (Electric Power Research Institute, 1993), which predicts a generally faster increase in γ_r with depth compared to the Darendeli (2001) relationship (see Fig. 4).

First, we consider simulations using upper and lower bound models of the reference strain. At the reference strain for which $G/G_{\max} = 0.5$, the standard deviation defined in the shear modulus reduction curves by Darendeli (2001) simplifies to

$$\sigma = \exp(\phi_{13}) + \sqrt{\frac{0.25}{\exp(\phi_{14})}} = 0.09638. \qquad (11)$$

Without PWP effects (PI = 0, OCR = 4), subtracting one standard deviation results in a reference strain that is slightly lower than that obtained with effective confining pressure (including pore water effects, Fig. 4). Adding one standard deviation (PI = 0) results in virtually the same reference strain obtained using PI = 20 with PWP effects. These results show that reference strains including plus or minus one standard deviation represent viable choices for the sediments of the San Bernardino and San Gabriel basins.

Figure 6 compares ground motions inside a rectangular region surrounding the largest patch of waveguide amplification inside the Los Angeles and San Gabriel basins, obtained from different nonlinear parameter assumptions. Adding one standard deviation to the reference strain given by the Darendeli relationship increases SA-3s to values above 0.4g inside large parts of the waveguide. Long-period ground motions obtained using the EPRI curves are slightly larger than those from the Darendeli relationship plus one standard deviation, but remain mostly below 0.5g. If we subtract one standard deviation from the reference strain obtained from Darendeli's relationship, the waveguide almost disappears from the ground-motion maps, with SA-3s generally below 0.3g.

To assess how the use of an oversimplified nonlinear model affects ground motions, we also carried out a nonlinear simulation using a single von Mises yield surface. The yield stress $\tau_{\max}$ of the yield surface was defined as the stress at the reference strain in the hyperbolic model, which corresponds to $\tau_{\max} = 0.5 \, \gamma_r \, G$, with the reference strain computed from Darendeli's relationship (PI = 0, no PWP). SA-3s values obtained using a single von Mises yield surface are lower than those obtained in the linear case but about twice the values obtained using the EPRI curves. The analysis shown here (Fig. 6) allows a direct comparison of the von Mises and Iwan models, because we used the same reference strain to calibrate the yield stress of the yield surface(s) in both the cases. Our results for the waveguide in the ShakeOut scenario shows that the multisurface Iwan model reduces ground motions by up to a factor of 2 compared to the single-yield surface model. Thus, assuming that the nonlinear parameters are reasonably
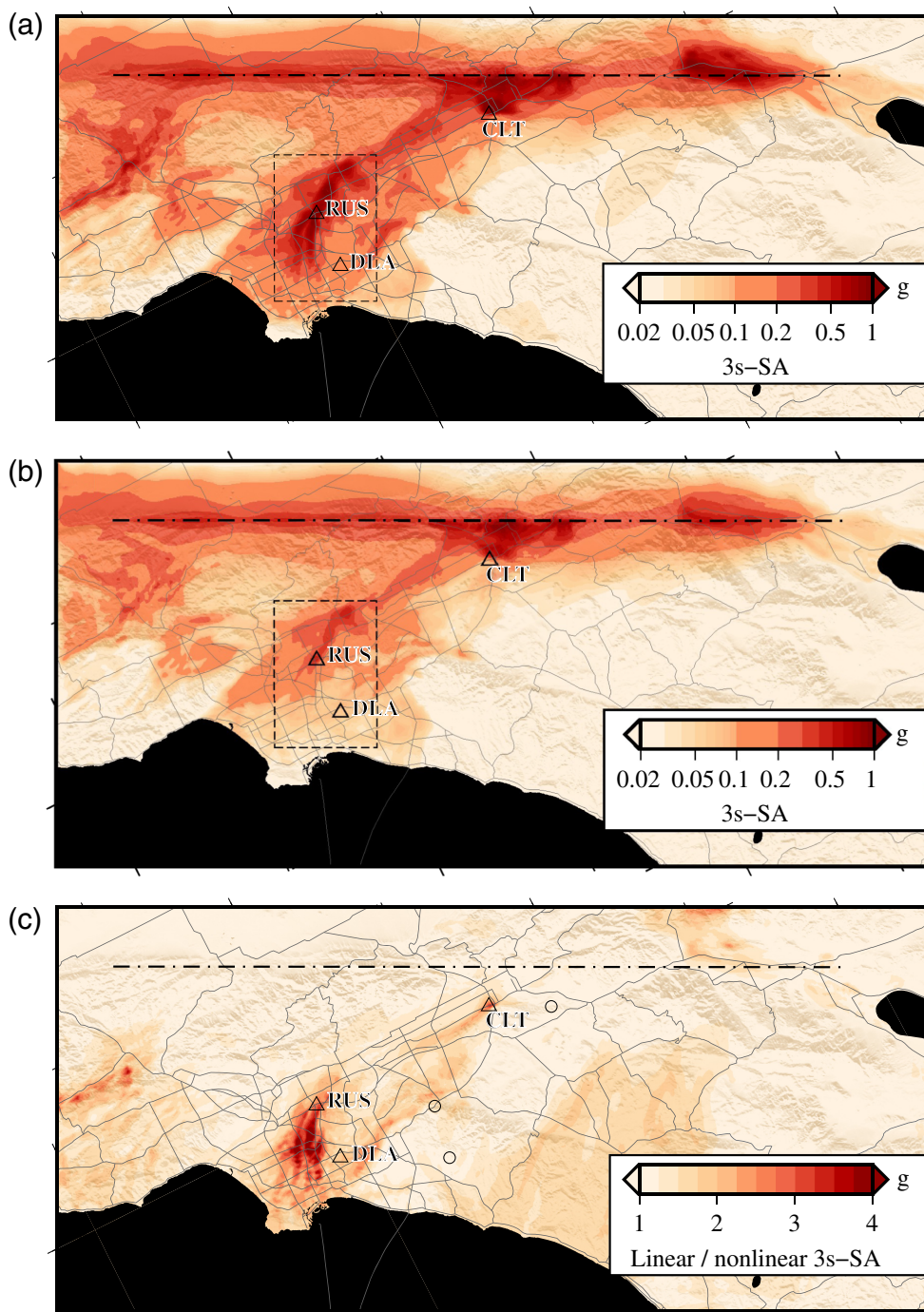
Figure 5. Spectral accelerations at a period of 3 s (SA-3s) obtained from dynamic simulation of the ShakeOut scenario for (a) linear and (b) nonlinear cases using the Iwan model and reference strains defined by the Darendeli (2001) relationship (PI = 0, OCR = 4, no PWP; Fig. 4). (c) Ratio between (a) linear and (b) nonlinear 3s-SAs. The rectangle shows the extent of the map region in Figure 6. The color version of this figure is available only in the electronic edition.

and DLA (downtown Los Angeles), illustrating how peak ground velocities (PGVs) decrease with decreasing values for the reference strain in the sediments (see Fig. 5b for station locations). The effects of plasticity are especially pronounced close to the SSAF, at site CLT, and inside the main waveguide at site RUS. FAS of the linear, von Mises, and Iwan multisurface solutions at the three sites, relative to the values at surrounding rock sites, confirm these conclusions (see Fig. S10).

It it worth noting that Iwan nonlinearity does not only affect ground-motion amplitudes but also the arrival times of strong-motion phases. For example, the largest peak along N180°E reaches Los Angeles about ∼0.5 s later in the Iwan model compared to the linear and bilinear solutions (Fig. 7). This shift is a direct consequence of the shear modulus reduction inside the low-velocity sediments of the basins during strong shaking, which is not captured using a bilinear solution.

SIMULATION ACCURACY, PERFORMANCE, AND SCALABILITY

AWP-ODC-Iwan keeps track of the minimum shear modulus (defined as the sum of the shear moduli associated with all nonyielding elements) encountered at each node during the simulation. Figure 8 (top, left) shows the minimum value of the shear modulus G, normalized by the low-strain shear modulus G_{max}, at the surface of the domain to a depth of 900 m for the ShakeOut simulation calculated with 20 yield surfaces. The value of G/G_{max} can only assume as many different values as the number of yield surfaces. In our ShakeOut scenario, the shear modulus

well constrained, the von Mises bilinear methodology produces up to twice the SA-3s values as compared to the multisurface yield model for the ShakeOut scenario.

Figure 7 shows synthetic seismograms extracted for the strongmotion sites CLT (Colton), RUS (Whittier-Narrows),

Simulation of ShakeOut scenario with Iwan nonlinearity

| Linear | von Mises Darendeli | Iwan EPRI curves | Iwan Darendeli ($+\sigma$) | Iwan Darendeli | Iwan Darendeli ($-\sigma$) |

g

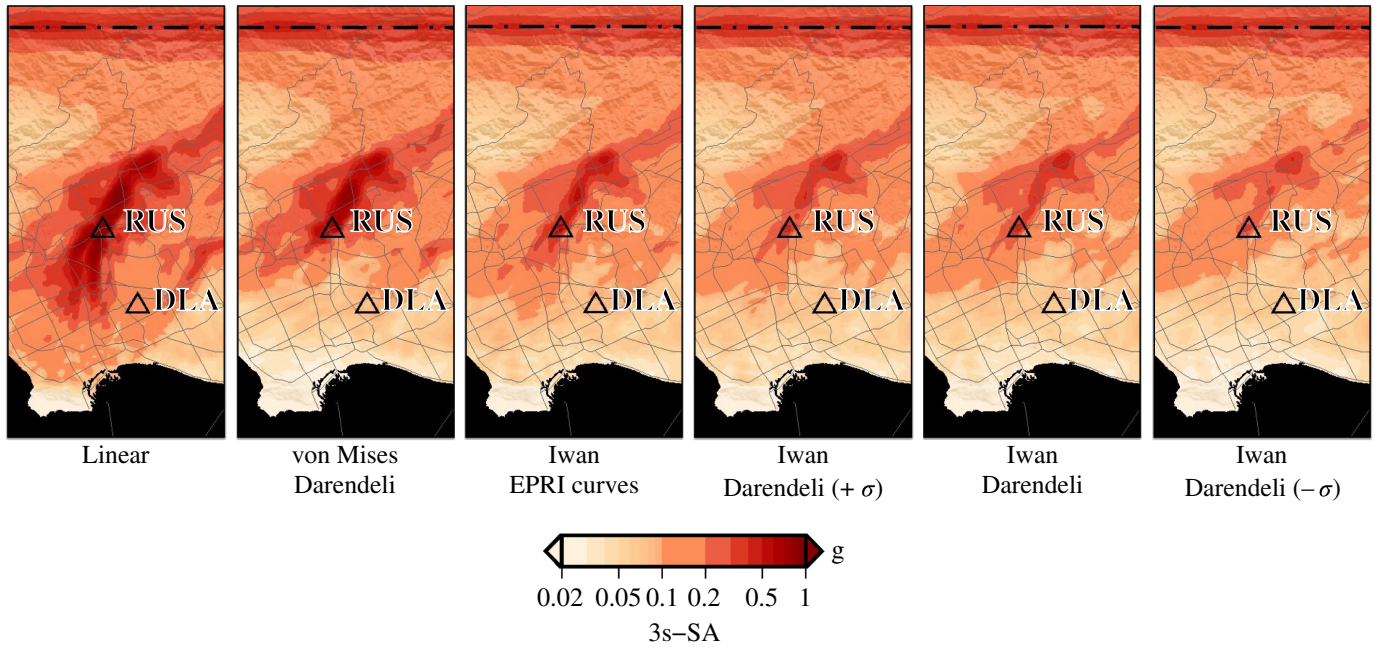0.02 0.05 0.1 0.2   0.5   1

3s−SA

Figure 6. SA-3s inside the rectangular area including the main waveguide amplification patch (Fig. 5) obtained in the linear case, the nonlinear case using a single von Mises yield surface, and a multisurface Iwan model using different definitions of the reference strain. The color version of this figure is available only in the electronic edition.
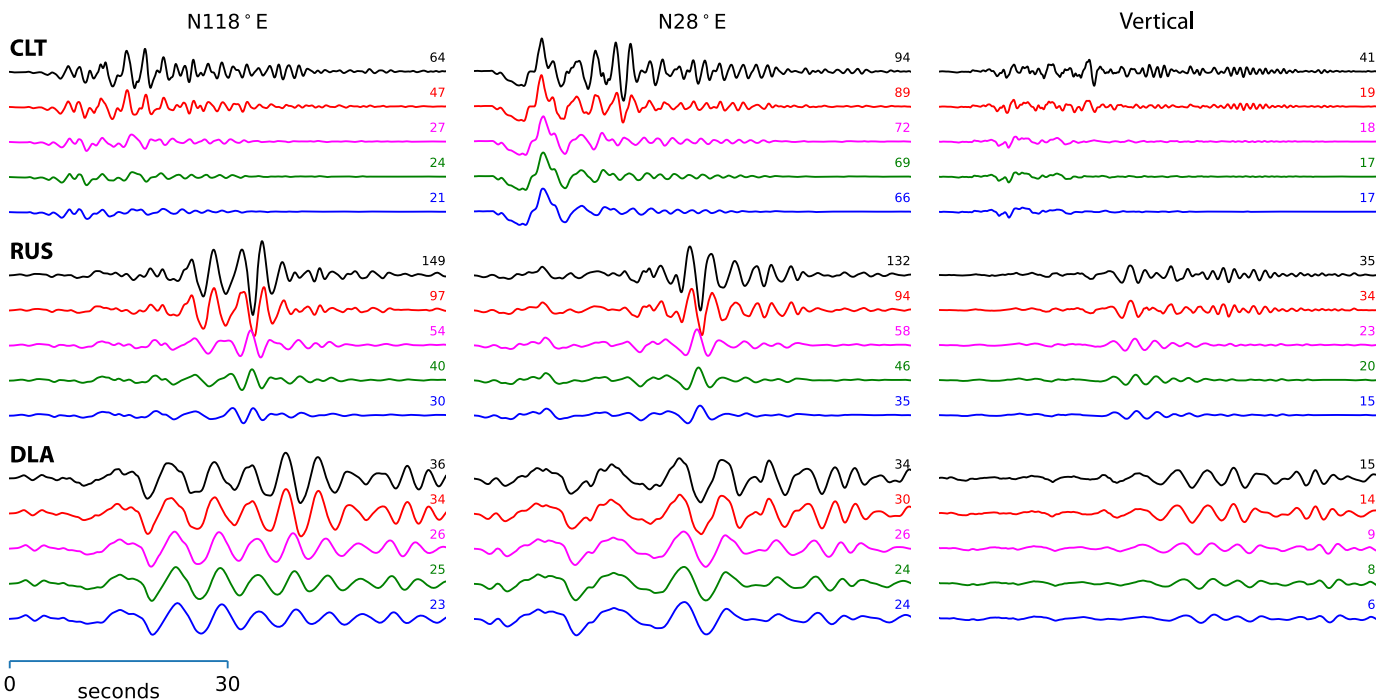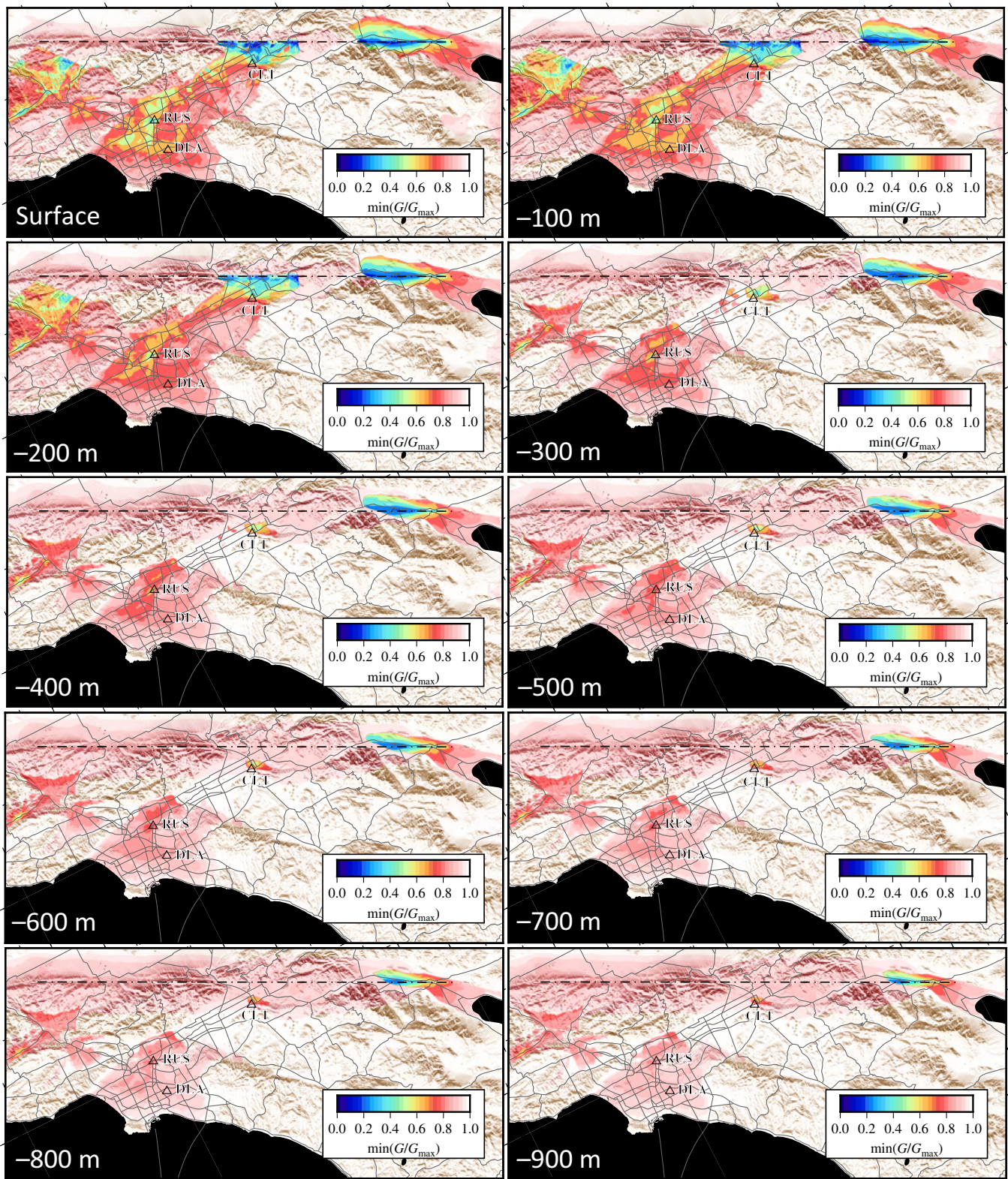

Figure 7. Synthetic seismograms computed at the strong-motion sites clt, rus, and dla from dynamic simulation of the ShakeOut scenario using (from top to bottom) a linear model, a single von Mises yield surface, and the Iwan model with: Darendeli reference strain plus 1 standard deviation, Darendeli reference strain, and Darendeli reference strain minus 1 standard deviation. See Figure 5 for station locations. Numbers above traces on the right indicate peak velocity in centimeters per second. The color version of this figure is available only in the electronic edition.

Figure 8. The minimum value of shear modulus *G*, normalized by the low-strain shear modulus G_{max}, at depths of 0–900 m encountered during the ShakeOut simulation. The color version of this figure is available only in the electronic edition.
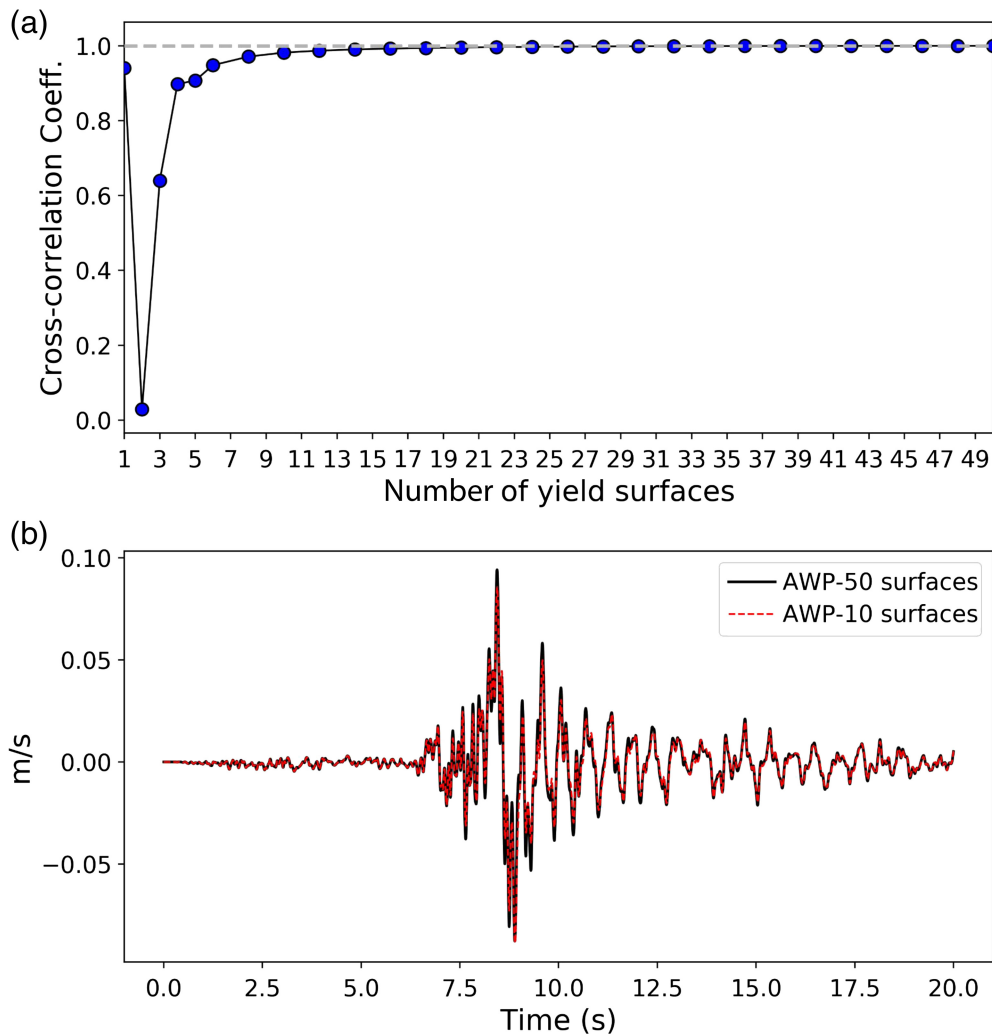
is reduced at the surface by about 75% where the SSAF intersects the low-velocity sediments of the San Bernardino basin and reaches values close to zero (i.e., all elements yield) in a few localized areas. The ~30 km long stretch with a G/G_{max} value of 50% marks the main waveguide along the Whittier Narrows corridor, which connects the San Gabriel basin with

Figure 9. (a) Cross-correlation coefficient between the waveforms obtained with 1–50 yield surfaces, relative to that for 50 yield surfaces for the 1D verification case. (b) Comparison of synthetic waveforms computed with 10 (dashed) and 50 (solid) yield surfaces. The color version of this figure is available only in the electronic edition.

As expected, the largest G/G_{max} reductions occur in the very near surface and decrease with depth (Fig. 8). The large reductions in G/G_{max} at the surface where the SSAF ruptures along the northeastern border of the San Bernardino basin are mostly eliminated below about 300 m depth, except for a localized area around station CLT. In the waveguide (e.g., station RUS), G/G_{max} values persist to about 0.7–0.9 at a depth of 900 m, similar to the values in the LA basin and most of the area surrounding the SSAF. The only location in the model where G/G_{max} values persist to values of 0.2–0.3 below a depth of 300 m is in Coachella valley near the epicentral area, where the fault intersects low-velocity sediments.

The accuracy of the Iwan rheology increases with the number of yield surfaces, which may be chosen based on specific needs and available computational resources. To guide this choice, Figure 9a shows the cross correlation between waveforms obtained for the 1D benchmark with 1–50 yield surface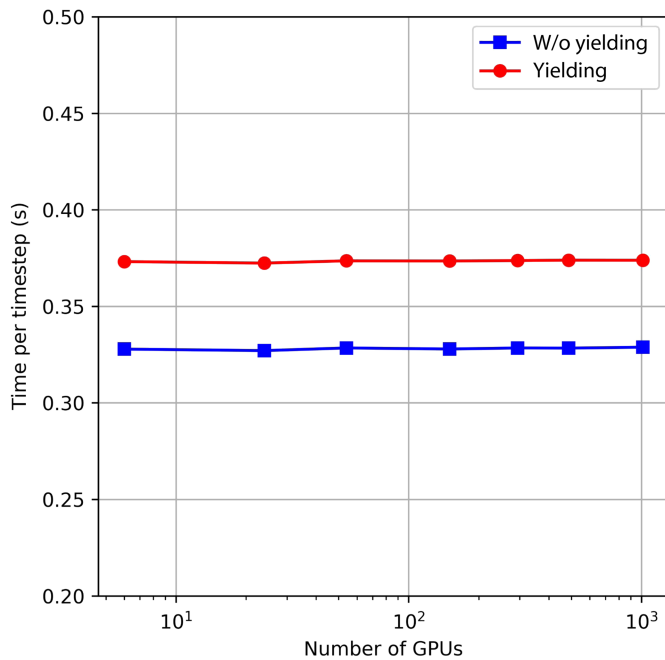s relative to that computed with 50 yield surfaces. The accuracy of the solution improves significantly up to about 10 yield surfaces, whereas additional surfaces only contributes minor improvement (see Fig. 9b). This result is again confirmed in the ShakeOut scenario; Figure S9 shows the SA-3s at the surface for a simulation using 20 rather than 10 (Fig. 5) yield surfaces. It is clear that the pattern of SA-3s is similar for the simulations with 10 and 20 yield surfaces, with additional details in the latter.

To assess the performance and the scalability of the Iwan implementation, we carried out a weak scaling test using the GPU version of AWP-ODC-Iwan on Summit at Oak Ridge Computing Facility. In this test, each GPU performed Iwan calculations with 10 yield surfaces for a model block with 160 $(x) \times 160$ $(y) \times 480$ (z) grid points, which nearly occupied the memory of a single GPU. The model has a grid spacing of 2 m, a timestep of 0.00015 s, and a 1D four-layer velocity structure identical to the sediment–bedrock layers used in the 2D benchmark (see properties in Table 2). A vertically incident

the LAB. Because simulations were carried out using a grid spacing of $\Delta h = 100$ m and the minimum shear-wave velocity of 500 m/s, only frequencies up to 1 Hz can be resolved in the linear case. Because the shear modulus degradation reduces the effective shear-wave velocity, the frequency limit will be reduced in the simulations with the Iwan rheology. For example, if the shear-modulus is reduced to 25% of G_{max}, the shear-wave velocity $V_S = \sqrt{G/\rho}$ is reduced to 50%, and the frequency limit is reduced to 0.5 Hz. To account for this effect, the minimum number of points per wavelength should be increased a priori, as pointed out by Bonilla *et al.* (2005), because the effective shear modulus reduction is only known after the simulation is completed. Although our Iwan-model results for the ShakeOut scenario using SA-3s are sufficiently resolved in almost the entire model area, future simulations with AWP-ODC-Iwan should anticipate the reduction in G/G_{max} due to nonlinear effects, and define grid spacing and/or maximum frequency accordingly.

Figure 10. Average run times needed for a single timestep for different numbers of graphic processing units (GPUs) measured from a weak scaling test for a scenario with very little yielding (squares) and one with substantial nonlinear yielding in materials at shallow depths (circles). The color version of this figure is available only in the electronic edition.

plane-wave source was inserted 30 m below the interface between the bedrock (bottom layer) and the third layer. The source time function was a delta function, low-pass filtered to frequencies below 10 Hz with identical velocity time history in all three directions. The weak scaling test was done by expanding the model size horizontally, as the number of GPUs increased proportionally to keep the workload of each GPU constant. Because the amount of calculations for each GPU depends on the yielding status of the layers, the run time is expected to increase as more yield surfaces may yield due to large ground motions. Figure 10 demonstrates the performance of the code in terms of the average run time per timestep for weak motion (average time for the first 200 timesteps, no yielding), and strong motion (average time for the first 4000 timesteps, widespread yielding). The extra workload due to extensive yielding leads to a ~15% average increase per timestep while the scalability remains constant. The good scalability for our AWP-ODC-Iwan implementation shows promise for large-scale simulations with higher frequencies.

The required computational memory increases with the number of yield surfaces chosen. Because six stress components and six memory variables associated with all individual yield surfaces need to be tracked and updated, users can expect an increase in memory consumption for each processor by a factor of $(1 + 0.4 \times Nspr)$ relative to that of a linear simulation, in which Nspr is the number of yield surfaces (e.g., a factor of 5 increase with 10 yield surfaces).

Finally, we note that our Von Mises multisurface implementation as proposed by Kaklamanos *et al.* (2015) accounts for static pressure dependence on the yield strength only, as is the case for the Noah and Noah2D codes used for verification. We encourage extension of the multisurface method in future work to include dynamic pressure dependence on the yield strength, which may play an important role in some cases, such as dynamic rupture simulations.

DISCUSSION AND CONCLUSIONS

We have implemented and verified support for hysteretic nonlinear rheology in the high-order scalable AWP-ODC finite-difference code using the parallel-series Iwan approach (Iwan, 1967). The implementation is successfully verified against 1D and 2D *SH*-wave benchmarks with realistic nonlinear parameters. Simulation of an *M* 7.8 earthquake on the SSAF (a variation of the ShakeOut scenario with a spontaneous rupture source) using AWP-ODC-Iwan shows that SAs-3s are reduced from 1*g* in the linear case to about 0.8 and 0.3–0.4*g* using 1 and 10 yield surfaces, respectively, in the region affected by waveguide amplification, depending on the choice of reference strain. Thus, if our chosen hyperbolic modulus reduction model and reference strain profiles are reasonable approximations to the response of the in situ materials, then the bilinear (von Mises) approximation of the rheology will significantly overpredict ground-motion levels in areas of amplification. In the SSAF scenario, the maximum overprediction may be on the order of a factor of 2, even allowing for estimated uncertainties in the reference-strain model. Shear modululus degradation in the waveguide reduces the maximum frequency that can be resolved in simulations with Iwan nonlinearity. A weak scaling test of AWP-ODC-Iwan with 10 yield surfaces showed that the code scales well on up to 1024 V100 GPUs.

We estimated the uncertainty of the ground motions for the ShakeOut scenario by one standard deviation of the reference strain from the Darendeli (2001) values, leading to variation of the PGVs in the waveguide (station RUS) by about 25%. Future work should further refine the effects of uncertainty on the PI and pore pressure on the resulting ground motions.

DATA AND RESOURCES

The simulations were performed on Summit and Andes at the Oak Ridge Leadership Computing Facility in Tennessee. Most of the data-processing work was done using Python and the Generic Mapping Tools (GMT) package (https://www.generic-mapping-tools.org). The velocity model for the 1D benchmark (KiK-net site KSRH10) can be found at http://prenolin.org). The 1D and 2D benchmarks are available at doi: 10.5281/zenodo.7502652. Noah and Noah2D were obtained from Fabian Bonilla (personal comm., 2018). AWP-ODC-Iwan is available upon request from Kim Olsen. All websites were last accessed in December 2022. The supplemental material contains additional figures illustrating the multisurface Iwan nonlinear method, a flow chart describing the implementation, details of the 1D and 2D verifications,

a SA-3s map of the ShakeOut scenario from a simulation with 20 yield surfaces, and spectral ratios at the three sites for the ShakeOut scenario.

DECLARATION OF COMPETING INTERESTS

The authors acknowledge that there that are no conflicts of interest recorded.

ACKNOWLEDGMENTS

REFERENCES

Amorosi, A., D. Boldini, and A. di Lernia (2016). Seismic ground response at Lotung: Hysteretic elasto-plastic-based 3D analyses, *Soil Dynam. Earthq. Eng.* **85,** 44–61.

Andrews, D. (2005). Rupture dynamics with energy loss outside the slip zone, *J. Geophys. Res.* **110,** no. B1, doi: 10.1029/2004JB003191.

Andrews, D., T. Hanks, and J. Whitney (2007). Physical limits on ground motion at Yucca Mountain, *Bull. Seismol. Soc. Am.* **97,** no. 6, 1771–1792.

Bethke, C. (1986). Inverse hydrologic analysis of the distribution and origin of Gulf Coast-type geopressured zones, *J. Geophys. Res.* **91,** no. B6, 6535–6545.

Bielak, J., R. Graves, K. Olsen, R. Taborda, L. Ramírez-Guzmán, S. Day, G. Ely, D. Roten, T. Jordan, P. Maechling, *et al.* (2010). The ShakeOut earthquake scenario: Verification of three simulation sets, *Geophys. J. Int.* **180,** no. 1, 375–404.

Blanc, E., G. Chiavassa, and B. Lombard (2013). A time-domain numerical modeling of two-dimensional wave propagation in porous media with frequency-dependent dynamic permeability, *J. Acoust. Soc. Am.* **134,** no. 6, 4610–4623.

Bonilla, L., R. Archuleta, and D. Lavallee (2005). Hysteretic and dilatant behavior of cohesionless soils and their effects on nonlinear site response: Field data observations and modeling, *Bull. Seismol. Soc. Am.* **95,** no. 6, 2373–2395.

Bonilla, L., P.-C. Luis, and S. Nielsen (2006). 1D and 2D linear and nonlinear site response in the Grenoble area, *Third International Symposium on the Effects of Surface Geology on Seismic Motion*, Grenoble, France, 30 August–1 September 2006, 82 pp.

Bradley, B. A. (2018). On-going challenges in physics-based ground motion prediction and insights from the 2010–2011 Canterbury and 2016 Kaikoura, New Zealand earthquakes, *Soil Dynam. Earthq. Eng.* **124,** 354–364.

Castro-Cruz, D., J. Regnier, E. Bertrand, and F. Courboulex (2020). A new parameter to empirically describe and predict the non-linear seismic response of sites derived from the analysis of Kik-Net database, *Soil Dynam. Earthq. Eng.* **128,** 105833, doi: 10.1016/j.soildyn.2019.105833.

Cerjan, C., D. Kosloff, and M. Reshef (1985). A nonreflecting boundary condition for discrete acoustic and elastic wave equations, *Geophysics* **50,** 705–708.

Chiang, D.-Y. (1992). Parsimonious modeling of inelastic systems, *Ph.D. Thesis*, California Institute of Technology, Pasadena, California.

Chiang, D., and J. Beck (1994). A new class of distributed-element models for cyclic plasticity-I. Theory and application, *Int. J. Solids Struct.* **31,** no. 4, 469–484.

Crouse, C., T. Jordan, K. Milner, C. Goulet, S. Callaghan, and R. Graves (2018). Site-specific MCER response spectra for los angeles region based on 3-D numerical simulations and the NGA West2 equations, *Eleventh U.S. National Conf. on Earthquake Engineering*, Los Angeles, California, 25–29 June.

Cui, Y., K. Olsen, K. Lee, J. Zhou, P. Small, D. Roten, G. Ely, D. Panda, A. Chourasia, J. Levesque, *et al.* (2010). Scalable earthquake simulation on petascale supercomputers, *Proc. of SC10*, New Orleans, Louisiana, 13–19 November.

Cui, Y., E. Poyraz, K. Olsen, J. Zhou, K. Withers, S. Callaghan, J. Larkin, C. Guest, D. Choi, A. Chourasia, *et al.* (2013). Physics-based seismic hazard analysis on petascale heterogeneous supercomputers, *Proc. of the International Conf. on High Performance Computing, Networking, Storage and Analysis*, ACM, 70 pp.

Dalguer, L., and S. Day (2007). Staggered-grid split-node method for spontaneous rupture simulation, *J. Geophys. Res.* **112,** no. B2, doi: 10.1029/2006JB004467.

Darendeli, M. B. (2001). Development of a new family of normalized modulus reduction and material damping curves, *Ph.D. Thesis*, The University of Texas at Austin, Austin, Texas.

Dawson, E., W. Roth, and B. Su (2013). 3-D Masing behavior of a parallel Iwan model, *IACGE 2013: Challenges and Recent Advances in Geotechnical and Seismic Research and Practices*, ASCE, 549–556.

de la Puenta, J., M. Dumbser, M. Kaeser, and H. Igel (2008). Discontinuous Galerkin methods for wave propagation in poroelastic media, *Geophysics* **73,** T77.

Delépine, N., L. Lenti, G. Bonnet, and J.-F. Semblat (2009). Nonlinear viscoelastic wave propagation: An extension of nearly constant attenuation (NCQ) models, *J. Eng. Mech.* **135,** no. 11, 1305–1314.

Denolle, M., E. Dunham, G. Prieto, and G. Beroza (2013). Strong ground motion prediction using virtual earthquakes, *Science* **343,** 399–403.

Duan, B., and S. Day (2010). Sensitivity study of physical limits on ground motion at Yucca Mountain, *Bull. Seismol. Soc. Am.* **100,** no. 6, 2996–3019.

Einav, I. (2005). A second look at strain space plasticity and latest applications, *Proc. of the 18th Australian Conf. on the Mechanics of Structures and Materials (ACMSM)*, Perth, Australia, Vol. 1, 225–231.

Einav, I., and I. Collins (2008). A thermomechanical framework of plasticity based on probabilistic micromechanics, *J. Mech. Mater. Struct.* **3,** no. 5, 867–892.

Electric Power Research Institute (1993). Guidelines for determining design basis ground motions, *Electric Power Research Institute Technical Rept. EPRI TR-102293*, available at https://www.epri.com/research/products/TR-102293-V5 (last accessed August 2023).

Gabriel, A.-A., J.-P. Ampuero, L. A. Dalguer, and P. M. Mai (2013). Source properties of dynamic rupture pulses with off-fault plasticity, *J. Geophys. Res.* **118,** no. 8, 4117–4126, doi: 10.1002/jgrb.50213.

Gottschämmer, E., and K. Olsen (2001). Accuracy of the explicit planar free-surface boundary condition implemented in a fourth-order staggered-grid velocity-stress finite-difference scheme, *Bull. Seismol. Soc. Am.* **91,** no. 3, 617.

Graves, R. W., B. T. Aagaard, K. W. Hudnut, L. M. Star, J. P. Stewart, and T. H. Jordan (2008). Broadband simulations for Mw 7.8 southern San Andreas earthquakes: Ground motion sensitivity to rupture speed, *Geophys. Res. Lett.* **35,** L22302, doi: 10.1029/2008GL035750.

Graves, R., T. Jordan, and S. E. A. Callaghan (2010). A physics-based seismic hazard model for Southern California, *Pure Appl. Geophys.* **168,** 367–381.

Griffith, D., and J. Prevost (1988). Two- and three-dimensional dynamic finite element analyses of the Long Valley Dam, *Geotechnique* **38,** 367–388.

Hardin, B., and V. Drnevich (1972). Shear modulus and damping in soils: Design equations and curves, *J. Soil Mech. Found. Div.* **98,** no. sm7, 667–692.

Harris, R., M. Barall, B. Aagaard, S. Ma, D. Roten, K. Olsen, B. Duan, D. Liu, B. Luo, K. Bai, *et al.* (2018). A suite of exercises for verifying dynamic earthquake rupture codes, *Seismol. Res. Lett.* **89,** 1146–1162.

Harris, R., M. Barall, R. Archuleta, E. Dunham, B. Aagaard, J. Ampuero, H. Bhat, V. Cruz-Atienza, L. Dalguer, P. Dawson, *et al.* (2009). The SCEC/USGS dynamic earthquake rupture code verification exercise, *Seismol. Res. Lett.* **80,** no. 1, 119–126.

Harris, R. A., M. Barall, D. Andrews, B. Duan, S. Ma, E. Dunham, A.-A. Gabriel, Y. Kaneko, Y. Kase, B. Aagaard, *et al.* (2011). Verifying a computational method for predicting extreme ground motion, *Seismol. Res. Lett.* **82,** no. 5, 638–644.

Iai, S., Y. Matsunaga, and T. Kameoka (1992). Strain space plasticity model for cyclic mobility, *Soils Found.* **32,** no. 2, 1–15.

Iwan, W. (1967). On a class of models for the yielding behavior of continuous and composite systems, *J. Appl. Mech.* **34,** no. 4, 612–617.

Jones, L. M., R. Bernknopf, D. Cox, J. Goltz, K. Hudnut, D. Mileti, S. Perry, D. Ponti, K. Porter, M. Reichle, *et al.* (2008). The ShakeOut scenario, *U.S. Geol. Surv. Open-File Rept. 2008-1150,* available at https://pubs.usgs.gov/of/2008/1150/ (last accessed August 2023).

Joyner, W. B. (2000). Strong motion from surface waves in deep sedimentary basins, *Bull. Seismol. Soc. Am.* **90,** no. 6B, S95–112, doi: 10.1785/0120000505.

Kaklamanos, J., L. Dorfmann, and L. G. Baise (2015). A simple approach to site-response modeling: The overlay concept, *Seismol. Res. Lett.* **86,** no. 2A, 413–423.

Kaneko, Y., and Y. Fialko (2011). Shallow slip deficit due to large strike-slip earthquakes in dynamic rupture simulations with elasto-plastic off-fault response, *Geophys. J. Int.* **186,** no. 3, 1389–1403.

Kramer, S. L. (1996). *Geotechnical Earthquake Engineering,* Prentice Hall, Hoboken, New Jersey.

Ma, S. (2008). A physical model for widespread near-surface and fault zone damage induced by earthquakes, *Geochem. Geophys. Geosys.* **9,** no. 11, Q11009, doi: 10.1029/2008GC002231.

Marcinkovich, C., and K. Olsen (2003). On the implementation of perfectly matched layers in a three-dimensional fourth-order velocity-stress finite difference scheme, *J. Geophys. Res* **108,** 2276.

Masing, G. (1926). Eigenspannungen und Verfestigung beim Messing, *Proc.of the 2nd Int. Congress of Applied Mechanics,* Zürich, Switzerland, Vol. 332 (in German).

Mroz, Z. (1967). On the description of anisotropic workhardening, *J. Mech. Phys. Solids* **15,** no. 3, 163–175.

Nelson, R., and A. Dorfmann (1995). Parallel elastoplastic models of inelastic material behavior, *J. Eng. Mech.* **121,** no. 10, 1089–1097.

Nowick, A., and B. Berry (1972). *Anelastic Relaxation in Crystalline Solids,* Academic Press, New York, New York.

Olsen, K., and R. Archuleta (1996). Three-dimensional simulation of earthquakes on the Los Angeles fault system, *Bull. Seismol. Soc. Am.* **86,** no. 3, 575–596.

Olsen, K. B., S. M. Day, L. A. Dalguer, J. Mayhew, Y. Cui, J. Zhu, V. Cruz-Atienza, D. Roten, P. Maechling, T. Jordan, *et al.* (2009). ShakeOut-D: Ground motion estimates using an ensemble of large earthquakes on the southern San Andreas fault with spontaneous rupture propagation, *Geophys. Res. Lett.* **36,** L04303, doi: 10.1029/2008GL036832.

Olsen, K. B., S. M. Day, J. B. Minster, Y. Cui, A. Chourasia, M. Faerman, R. Moore, P. Maechling, and T. Jordan (2006). TeraShake: Strong shaking in Los Angeles expected from southern San Andreas earthquake, *Seismol. Res. Lett.* **77,** 281–282.

Olsen, K. B., S. M. Day, Y. A. Minster, Y. Cui, A. J. Chourasia, D. Okaya, and P. Maechling (2008). Terashake2; spontaneous rupture simulations of Mw 7.7 earthquakes on the southern San Andreas fault, *Bull. Seismol. Soc. Am.* **98,** no. 3, 1162–1185.

Rajaure, S., D. Asimaki, E. Thompson, S. Hough, S. Martin, J. Ampuero, M. Dhital, A. Inbal, N. Takai, M. Shigefuji, *et al.* (2017). Characterizing the Kathmandu Valley sediment response through strong motion recordings of the 2015 Gorkha earthquake sequence, *Tectonophysics* **714,** 146–157.

Régnier, J., L. Bonilla, P. Bard, H. Kawase, E. Bertrand, F. Hollender, M. Marot, D. Sicilia, and A. Nozu (2015). PRENOLIN Project: A benchmark on numerical simulation of 1D non-linear site effects. 2-Results of the validation phase, *6th International Conf. on Earthquake Geotechnical Engineering,* 1–4 pp.

Régnier, J., L. Bonilla, P.-Y. Bard, E. Bertrand, F. Hollender, H. Kawase, D. Sicilia, P. Arduino, A. Amorosi, D. Asimaki, *et al.* (2018). PRENOLIN: International benchmark on 1D nonlinear site-response analysis-validation phase exercise, *Bull. Seismol. Soc. Am.* **108,** no. 2, 876–900.

Regnier, J., L.-F. Bonilla, and P.-Y. Bard (2016). International benchmark on numerical simulations for 1D, nonlinear site response (PRENOLIN): Verification phase based on canonical cases, *Bull. Seismol. Soc. Am.* **106,** no. 5, 2112–2135.

Roten, D., Y. Cui, K. Olsen, S. Day, K. Withers, W. Savran, W. Peng, and D. Mu (2016). High-frequency nonlinear earthquake simulations on petascale heterogeneous supercomputers, *2016 ACM/IEEE International Conference for High Performance Computing, Networking, Storage and Analysis (SC'16),* Salt Lake City, Utah, 13–18 November 2016.

Roten, D., K. Olsen, Y. Cui, and S. Day (2017). Quantification of fault zone plasticity effects with spontaneous rupture simulations, *Pure Appl. Geophys.* **174,** 3369–3391, doi: 10.1007/s00024-017-1466-5.

Roten, D., K. Olsen, and S. Day (2017). Off-fault deformations and shallow slip deficit from dynamic rupture simulations with fault zone plasticity, *Geophys. Res. Lett.* **44,** 7733–7744.

Roten, D., K. Olsen, S. Day, and Y. Cui (2016). High-frequency nonlinear simulations of southern San Andreas earthquake scenarios, *SCEC 2016 Annual Meeting Proceeding and Abstracts,* Palm Springs, California, 11–14 September.

Roten, D., K. Olsen, S. Day, Y. Cui, and D. Fäh (2014). Expected seismic shaking in Los Angeles reduced by San Andreas Fault zone plasticity, *Geophys. Res. Lett.* **41,** no. 8, 2769–2777.

Roten, D., K. B. Olsen, J. Pechmann, V. Cruz-Atienza, and H. Magistrale (2011). 3D Simulations of M 7 earthquakes on the Wasatch fault, Utah, Part I: Long-period (0-1 Hz) ground motions, *Bull. Seismol. Soc. Am.* **101,** no. 5, 2045–2063.

Santisi d'Avila, M., and J.-F. Semblat (2014). Nonlinear seismic response for the 2011 Tohoku earthquake: Borehole records versus one-directional three-component propagation models, *Geophys. J. Int.* **197,** 566–580.

Santisi d'Avila, M., L. Lenti, S. Martino, and W. Romeo (2019). Nonlinear numerical simulation of the soil seismic response to the 2012 Mw 5.9 Emilia earthquake considering the variability of the water table position, *Bull. Seismol. Soc. Am.* **109,** no. 2, 505–524.

Santisi d'Avila, M., L. Lenti, and J.-F. Semblat (2012). Modeling strong seismic motion: Three-dimensional loading path versus wavefield polarization, *Geophys. J. Int.* **190,** 1607–1624.

Santisi d'Avila, M., J.-F. Semblat, and L. Lenti (2013). Modeling strong seismic motion: Three-dimensional loading path versus wavefield polarization, *Bull. Seismol. Soc. Am.* **103,** 1394–1410.

Schnabel, P., H. B. Seed, and J. Lysmer (1972). Modification of seismograph records for effects of local soil conditions, *Bull. Seismol. Soc. Am.* **62,** no. 6, 1649–1664.

Seed, H. B., and I. M. Idriss (1969). Influence of soil condition on ground motions during earthquakes, *J. Soil Mech. Found. Div.* **6347,** 99–137.

Simo, J. C., and R. L. Taylor (1986). A return mapping algorithm for plane stress elastoplasticity, *Int. J. Numer. Methods Eng.* **22,** no. 3, 649–670.

Sleep, N. H. (2010). Nonlinear behavior of strong surface waves trapped in sedimentary basins, *Bull. Seismol. Soc. Am.* **100,** no. 2, 826–832.

Sleep, N. H. (2014). Ambient tectonic stress as fragile geological feature, *Geochem. Geophys. Geosys.* **15,** no. 9, 3628–3644.

Sleep, N. H., and B. A. Erickson (2014). Nonlinear attenuation of S-waves and Love waves within ambient rock, *Geochem. Geophys. Geosys.* **15,** no. 4, 1419–1440.

Taborda, R., J. Bielak, and D. Restrepo (2012). Earthquake ground motion simulation including nonlinear soil effects under idealized conditions with application to two case studies, *Seismol. Res. Lett.* **83,** no. 6, 1047–1060.

Tu, T., H. Yu, L. Ramirez Guzman, J. Bielak, O. Ghattas, K. Ma, and D. O'Hallaron (2006). From mesh generation to scientific visualization: An end-to-end approach to parallel supercomputing, *Proc. of the 2006 ACM IEEE International Conference for High Performance Computing, Networking, Storage and Analysis*, IEEE Computer Society, Tampa, Florida, Vol. 73, 15 pp.

Wilkins, M. L. (1964). *Calculation of Elastic-Plastic Flow*, Vol. 3, Academic Press, New York, New York.

Withers, K., K. Olsen, and S. Day (2015). Memory efficient simulation of frequency dependent Q, *Bull. Seismol. Soc. Am.* **105,** 3129–3142.

Wollherr, S., A.-A. Gabriel, and P. M. Mai (2019). Landers 1992 "reloaded": Integrative dynamic earthquake rupture modeling, *J. Geophys. Res.* **124,** no. 7, 6666–6702.

Wollherr, S., A.-A. Gabriel, and C. Uphoff (2018). Off-fault plasticity in three-dimensional dynamic rupture simulations using a modal discontinuous Galerkin method on unstructured meshes: Implementation, verification and application, *Geophys. J. Int.* **214,** no. 3, 1556–1584.

Xu, J., J. Bielak, O. Ghattas, and J. Wang (2003). Three-dimensional nonlinear seismic ground motion modeling in basins, *Phys. Earth Planet. In.* **137,** nos. 1/4, 81–95.